ACS Photonics

Article

pubs.acs.org/journal/apchd5

Computational Design of Durable Spherical Nanoparticles with Optimal Material, Shape, and Size for Ultrafast Plasmon-Enhanced Nanocavitation

Rémi Lachaine,[†] Étienne Boulais,[†,‡] David Rioux,[†] Christos Boutopoulos,[†,§] and Michel Meunier*[,†]

[†]Polytechnique Montréal, Laser Processing and Plasmonics Laboratory, Department of Engineering Physics, Montréal, Québec H3C 3A7, Canada

[‡]Université de Montréal, Laboratory of Biosensors and Nanomachines, Department of Chemistry, Montréal, Québec H3C 3A7, Canada

[§]SUPA, School of Physics and Astronomy, University of St. Andrews, North Haugh, St. Andrews KY16 9SS, United Kingdom

Supporting Information

ABSTRACT: Photons interaction with metallic nanoparticles can excite a resonant plasmon that concentrates energy at the nanoscale. At high intensity, this quasi-particle decays into a photoexcited nanoplasma that triggers the generation of nanobubbles, which can be used for imaging and therapeutic purposes. This highly nonlinear wavelength-dependent process is controlled by the nanoparticle material, shape, and size in intricate ways, which justifies the need for a systematic design approach that currently lacks in the field. To palliate to this, we developed in this work a computational framework that enables the efficient in silico screening of large libraries of spherically symmetric structures and metallic materials. Using this framework, we have investigated the nanocavitation performance of spherical nanoparticles with more than 14 million combinations of materials, shapes, sizes, and irradiation conditions, from which we could distill general principles for the design of durable nanoantennas. In the near-infrared, our work suggests that Cu, TiN, Ag, and Au nanoparticles offer similar performance, with optimal diameters of $\sim\lambda/5$. In contrast, only Ag and Al are appropriate for irradiation in the UV−visible, cavitation being associated with structural damage for all other tested materials at these wavelengths. We also demonstrate that silica-metal nanoshell structures have the potential to reduce the cavitation threshold at all wavelengths compared to homogeneous nanoparticles due to their extensive spectral tunability. However, designing more complex layered systems seems to bring no benefit. Our work provides important physical insight on the influence of materials on nanocavitation and simulation-based design guidelines that should be broadly useful for the engineering of nonlinear nanoplasmonic materials for biological applications.

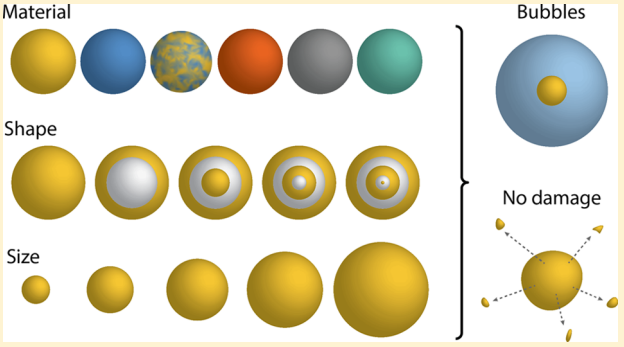

KEYWORDS: *bubble, ultrashort pulse, plasmonic nanoantenna, nanoshell, nanolens*

The engineering and synthesis of nanoplasmonic materials have recently enabled the design of nanoantennas of various sizes and shapes that can manipulate light at the nanoscale, well beyond the diffraction limit.[1−4] Silver (Ag) and gold (Au) are the most common metals for plasmonic structure synthesis, with applications ranging from tissue imaging[5−8] to light harvesting[4,9] and drug delivery.[10,11] However, plasmon excitation can exist in a large variety of materials, which could be exploited to develop new applications.

To efficiently sustain surface plasmon, the real part of the dielectric function ϵ_m of a given material should be negative, and much larger than its imaginary counterpart, the latter being associated with resistive losses.[12] A large variety of metals beyond Au and Ag possess these characteristics, including aluminum (Al), copper (Cu), nickel (Ni), platinum (Pt), titanium nitride (TiN), and gold−silver alloys (AuAg). These have recently drawn a lot of attention in the plasmonic community and have emerged as potential substitute to Au and Ag in many applications for which their specific band structure, catalytic properties or cost-effectiveness can be advantageously exploited. For instance, Al nanoparticles (NP) have been used to generate hot carriers for photovoltaic applications[13−15] and as photocatalyst for hydrogen dissociation.[16] Additionally, adequately removing oxide from CuNP have enabled replacing AgNP and AuNP in SERS imaging applications at a fraction of their price.[17] Other works have leveraged the catalytic properties of NiNP to enable the growth of carbon nanotubes[18,19] and have demonstrated the great potential of high-density PtNP dispersed in a carbon matrix for oxygen reduction

Received: August 29, 2016

DOI: 10.1021/acsphotonics.6b00652
ACS Photonics XXXX, XXX, XXX−XXX

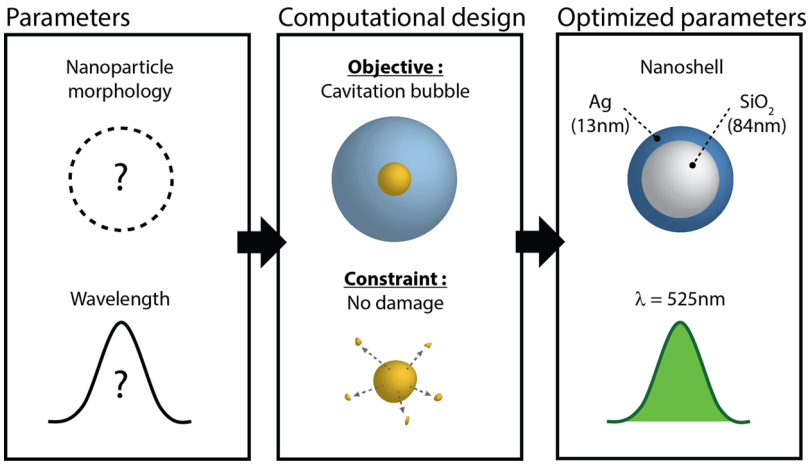

Figure 1. Optimization of irradiation condition and plasmonic nanomaterials for nanocavitation. An in silico procedure screens possible plasmonic material, nanostructure shapes, and irradiation wavelength to minimize the energy required for cavitation while avoiding damage to the NP.

and other electrocatalytic applications.[20] TiN can also present plasmonic properties[21,22] and TiNNP have been used to generate local heating.[23] Finally, our group has recently developed methods for tuning the dielectric function and plasmonic resonance peak of AuAg alloy NP with high precision,[24−26] enabling multiplexed tissue imaging.[27,28]

One particularly interesting application of nanoplasmonic is the possibility to create controllable nanoscale bubbles that can be used to precisely interact with live cells. In this work, we sought to optimize the production of nanobubbles around water-immersed plasmonic NP irradiated with ultrashort laser pulses (70 fs), using NP of different sizes, shapes, and compositions that had remained largely unexplored. We have previously demonstrated that the cavitation process in these conditions results from the nonlinear photoexcitation of a quasi-free electron density in the near-field, which energy is sufficient to induce explosive phase change and generate nanoscale bubbles around the particle upon relaxation.[29,30] This electron density, which can reach a temperature of thousands of kelvins with a lifetime of tens of picoseconds, is called plasma throughout this work. This hot plasma is generated directly in the water, not into the plasmonic metal, through multiphotonic excitation of water molecules, enabling the formation of nanobubbles with low NP light absorption. When targeting cells, these nanobubbles can transiently permeabilize the membrane to all sorts of molecular cargo, including DNA, RNA, and drug molecules, stimulating interest for applications in nanomedicine.[31−34]

To efficiently translate ultrafast plasmon-enhanced nanocavitation technology to a biological context, the laser energy surface density (fluence) required to trigger bubble production must be reduced as much as possible to limit collateral damage to surrounding cells and tissues. On the other hand, the energy directly absorbed by the particle from resistive losses must remain under a certain limit to ensure that the particle does not sustain irreversible damage, which would result in potentially toxic particle fragments[35] and would hinder repeatability and multipulses or scanning procedures. A delicate balance between plasmon excitation and near-field enhancement must therefore be reached by the careful design of nanoantennas in regards of shape, size, composition, and irradiation wavelength. Studies from other groups have previously tackled the optimization of near-field enhancement for plasma generation[36] but never considered the durability constraint, limiting their study to Au and Ag.

The shape, size, and dielectric function of the material that constitute the nanostructure modify the plasmonic response in highly intricate ways, which makes the design process complex and nontrivial, in particular, for nonlinear interactions. The systematic experimental synthesis and characterization of all possible nanoantennas and irradiation conditions would require formidable time and effort. In this work, we instead developed and used a high-throughput in silico procedure that enables screening rapidly and efficiently the extremely large library of all possible nanoparticle shapes, sizes, and composition under various irradiation conditions to design the best nanostructure for plasmon-enhanced cavitation (Figure 1). Previously, we have used a similar methodology to successfully optimize silica-gold nanoshells for cell optoporation in the near-infrared, demonstrating the relevance of the technique.[37] Building on this important validation, here, we considerably expand on this work and screen for a large variety of spherical shapes, including spherical particles (NP), nanoshells (NS), and *n*-layers multishell structures (*n*-MS, $n = 3-5$), composed from nine metals and alloys (Au, Ag, Al, Cu, TiN, Pt, Ni, Ti, and AuAg 50:50 alloys) for a total of 14 million combinations. These particles are optimized for a large selection of wavelengths (λ) across UV−visible (λ = 300−700 nm) and near-infrared (NIR; λ = 700−1000 nm) and total diameters from 1 to 200 nm, by evaluating their fluence thresholds for cavitation (F_{bubble}) and structural damage (F_{damage}).

Our results demonstrate that Cu, TiN, Ag, and Au NP all offer similar performance in the NIR and that only Al and Ag can be optimized in the UV−visible due to higher resistive losses for the other metals. Interestingly, we show that the size of the optimal NP irradiated in the NIR does not depend on the material, but only on the wavelength. Then, we demonstrate that the extended tunability of NS reduces F_{bubble} by up to 85%, especially in the NIR, and that only a marginal gain is obtained with *n*-MS, considerably reducing the interest for these more complex structures. Finally, we provide important guidelines for the design of nanomaterials for plasmon-enhanced nanocavitation, which should more generally enable the design of plasmonic nanostructures tailored to various nonlinear applications in cell and liquid environments.

DOI: 10.1021/acsphotonics.6b00652
ACS Photonics XXXX, XXX, XXX−XXX

RESULTS AND DISCUSSION

Computational Design Approach and Validation. First, we developed a simple model capable of predicting the laser fluence F_{bubble} required to induce cavitation around a spherical plasmonic nanoparticle of any materials and compositions. We have defined this cavitation threshold as the fluence needed to reach a critical plasma density of $\rho = 10^{21}$ cm^{-3} into the near-field enhancement of the nanostructure,[38−40] although lower values are also sometimes reported.[41] We calculated the plasma density from a rate equation (eq 1 in Methods) that considered the photoionization rate calculated using Keldysh theory, the collision rate for the impact ionization process, the diffusion rate of the plasma density leaving the near-field region and the recombination rate of the plasma relaxation.

To validate this cavitation model, we compared the computed F_{bubble} with previously published experimental cavitation threshold[42] obtained with the shadowgraphy technique for 50−250 nm AuNP irradiated with 70 fs, 800 nm laser pulses (Figure 2a). We observed that the general trend

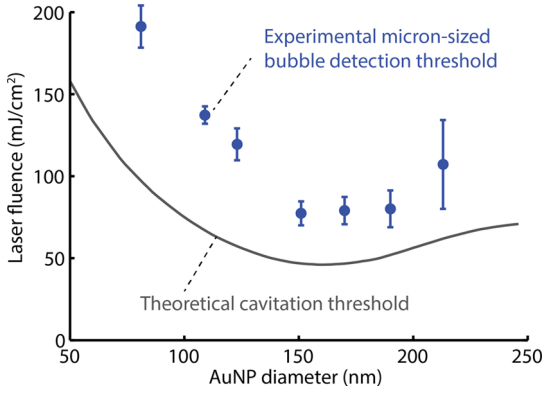

Figure 2. Validation of the computational design methodology. Micron-size bubble detection threshold and theoretical cavitation threshold based on an optical breakdown threshold as a function of AuNP diameter. As expected, the experimental results are slightly higher because of the larger bubble detection threshold.

of the experimental data is well reproduced. A systematic underestimation of the cavitation threshold is observed due to the fact the experimental observation concerns detectable bubble of size ∼1 μm, instead of the theoretical pointwise cavitation, the latter likely occurring at a slightly lower fluence. Similar results were previously obtained with AuNS.[37]

Second, we used a simple model to calculate the laser fluence F_{damage} required to damage the NP. Melting is commonly identified as the onset physical mechanism leading to NP structural shape modifications.[43,44] We have thus defined the damage threshold as the fluence needed to reach the melting temperature into the NP, considering its absorption cross-section and thermodynamic properties. Using this model, we estimated that the laser fluence required to reach melting temperature of a 100 nm AuNP was 370 mJ/cm^2, which is comparable to experimental damage threshold results of 315 ± 70 mJ/cm^2 in similar irradiation conditions.[45] We also estimated a damage threshold of 73 mJ/cm^2 for AuNS (39 nm silica core radius and 28 nm gold shell thickness), which is also comparable to previous experimental damage results of 65 ± 15 mJ/cm^2 in similar irradiation conditions.[37] Of course, nanostructure damage could occur at lower temperature than melting through other thermodynamic pathways such as spallation or phase explosion.[46−48] However, these mechanisms being rather difficult to assess, we decided to compensate for this slight difference by setting, as a factor of safety, that F_{damage} should be at least twice F_{bubble} to consider the particle as durable. This ensures that no structural damage occurs when bubble are generated.

Near-field enhancement and absorption cross-section of the particles have been calculated using Mie theory. Optimized nanostructures were defined as the durable particles that minimize F_{bubble}.

In summary, our simple model can yield a reasonable estimation of the cavitation fluence and the melting fluence in less than 0.1 s for a given irradiation condition using a standard personal computer. This remarkable rapidity has enabled to calculate more than 14 million irradiation conditions in a fairly reasonable amount of time. More complete models that can capture cavitation dynamics with greater accuracy have been recently developed by our group.[29,42] However, these models take at least an hour to calculate, and it would have been impossible to use them to test as many conditions in realistic amounts of time. The simple model presented in this paper is therefore very useful to rapidly screen large libraries of nanomaterials and irradiation conditions to unravel tendency and general principles, which is the purpose of the present paper.

Wavelength-Dependent Cavitation around 100 nm AuNP and Optimal Size of AuNP. To characterize the influence of the irradiation wavelength on plasmon-enhanced nanocavitation, we used our computational framework to evaluate the cavitation and structural damage thresholds for 100 nm AuNP irradiated with ultrashort laser pulses (70 fs) with wavelengths between 300 and 1000 nm. The wavelength of the incident photons has a major influence on the dynamic of plasma and bubble generation around the NP because of the highly nonlinear nature of the energy transfer process. In pure water, when no NP are present, the number of photons involved in multiphoton ionization varies from 3 photons at λ = 400 nm to 7 photons at λ = 1000 nm, creating well-defined steps in the wavelength evolution of F_{bubble} (Figure 3a), as previously reported by Linz et al.[49] In addition, when NP are present, the irradiation wavelength substantially influences the polarizability of the plasmonic structures, resulting in strong variations of the near-field enhancement and absorption cross-section (Figure 3b). The combination of these two phenomena (modification of the nonlinear order and particle polarizability) engenders slightly smoother steps for plasmon-enhanced F_{bubble} compared to cavitation in pure water, but still clearly shows unambiguous signature of nonlinearity (Figure 3c).

Using our computational approach, we show that 100 nm AuNPs are optimal for irradiation at λ = 651 nm, which offers the right balance between near-field enhancement and absorption cross-section, with $F_{bubble} \sim 31$ mJ/cm^2. At longer wavelength, reduced near-field enhancement coupled to higher-order nonlinear interaction increases F_{bubble}, while at shorter wavelength, increased absorption cross-section leads to structural damage. In this work, we require that F_{damage} is at least twice F_{bubble} as a factor of safety to consider that the nanoantenna is durable (green line in Figure 3c). Durable cavitation is thus suggested by our simulation results for the whole 651−1000 nm portion of the spectrum with this type of particle.

DOI: 10.1021/acsphotonics.6b00652
ACS Photonics XXXX, XXX, XXX−XXX

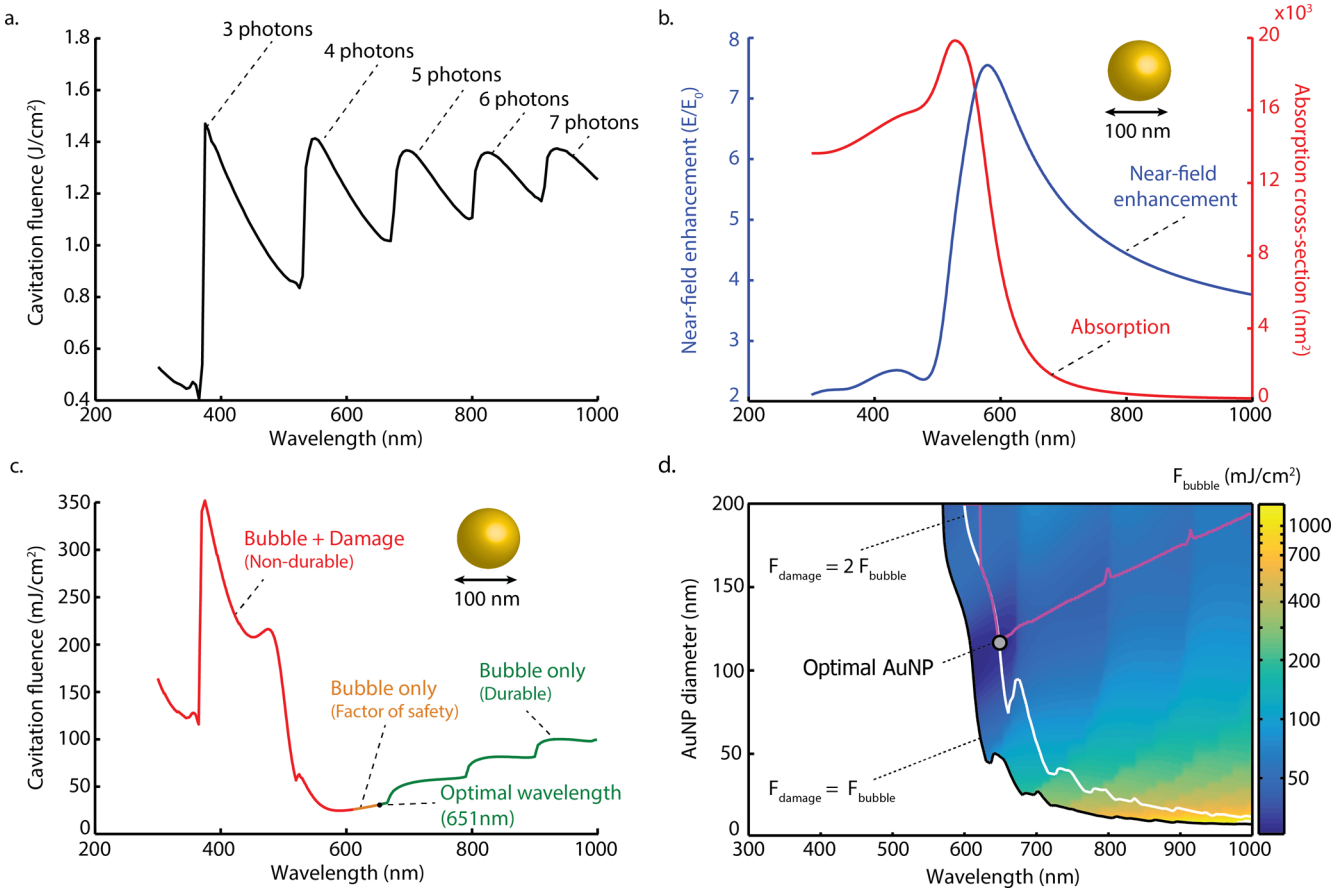

Figure 3. Wavelength-dependent plasmon-enhanced cavitation threshold with 100 nm AuNP and ultrashort laser pulses (70 fs). (a) Cavitation threshold in pure water (no NP) as a function of the irradiation wavelength. Each discrete step corresponds to a change in the number of photons required to photoionize water (band gap of 6.5 eV). (b) Near-field enhancement and absorption cross-section for a 100 nm AuNP in water as a function of the irradiation wavelength. (c) Cavitation threshold for 100 nm water-immersed AuNP. Red and green lines, respectively, correspond to regions where the NP sustain structural damage and remain intact. The orange line indicates a region where the melting fluence is less than twice the cavitation fluence threshold. (d) Fluence needed to reach cavitation without melting. The white area indicates a region where achieving durable cavitation is impossible. The white line shows the factor of safety boundary, a limit where the damage fluence is twice the cavitation fluence. The pink line indicates the diameter corresponding to the minimal fluence at each wavelength while still respecting the factor of safety.

Next, we investigated how tuning the size of AuNP could improve plasmon-enhanced cavitation. Results show that AuNP performance is slightly better for 115 nm AuNP compared to 100 nm AuNP, when irradiated at an optimal wavelength (λ = 645 nm, $F_{bubble} \sim 28$ mJ/cm^2; Figure 3d). Notably, at λ = 800 nm, the optimal AuNP diameter is 150 nm, in agreement with previous theoretical studies.[50] The wavelength window under which durable cavitation can occur is also slightly increased compared to 100 nm AuNP, covering the 600−1000 nm portion of the spectrum. At short wavelengths (600−650 nm), the optimal size is largely limited by AuNP absorption, as shown by the fact that the optimal diameter curve (pink line in Figure 3d) closely follows the damage threshold limit. In the NIR, because of reduced absorption, the optimal diameter (D) is fully determined by the maximization of the near-field enhancement. The maximal near-field enhancement can be roughly evaluated from the dipolar response of NP to electromagnetic field, and can be shown to occur for particles of diameters $D = 0.76\lambda/\pi n$ (Supporting Information (SI), Supporting Note 1), where n is the environment refractive index. For water (n = 1.33), this equation yield approximately $D \sim \lambda/5$. The existence of this maximum is a consequence of the balance between the damping of the polarizability due to dipolar emission, and the enhancement of that same dipole due to the volume increase.

Importance of the Choice of Materials for Optimal Plasmon-Enhanced Nanocavitation. While Au is certainly among the most popular plasmonic materials, together with Ag, several other metals share the dielectric function characteristics that are required to efficiently sustain surface plasmon. Using our computational framework, we have investigated how using other metals could improve plasmon-enhanced cavitation. We computed the optimal NP made of Ag, Cu, Al, TiN, Ni, Pt, Ti, and 50/50 gold−silver alloy (AuAg) for durable plasmon-enhanced nanocavitation (Figure 4a,b). Results show that, due to their distinct dielectric function and thermodynamic properties, each material leads to feasible designs for irradiation in limited portion of the spectra. For instance, compared to AuNP, AgNP increases the durable cavitation window by 54% to a much wider 384−1000 nm range. On the other hand, CuNP reduce this window to a region covering only wavelengths larger than 635 nm. Similarly, AlNP only covers a short region of the UV−visible spectrum (300−368 nm). Notably, PtNP, TiNP, and NiNP never lead to cavitation without sustaining damage across all the UV−visible and NIR range. AuAgNP and TiNNP have a very peculiar behavior, showing durable cavitation in disconnected regions of the

DOI: 10.1021/acsphotonics.6b00652
ACS Photonics XXXX, XXX, XXX−XXX

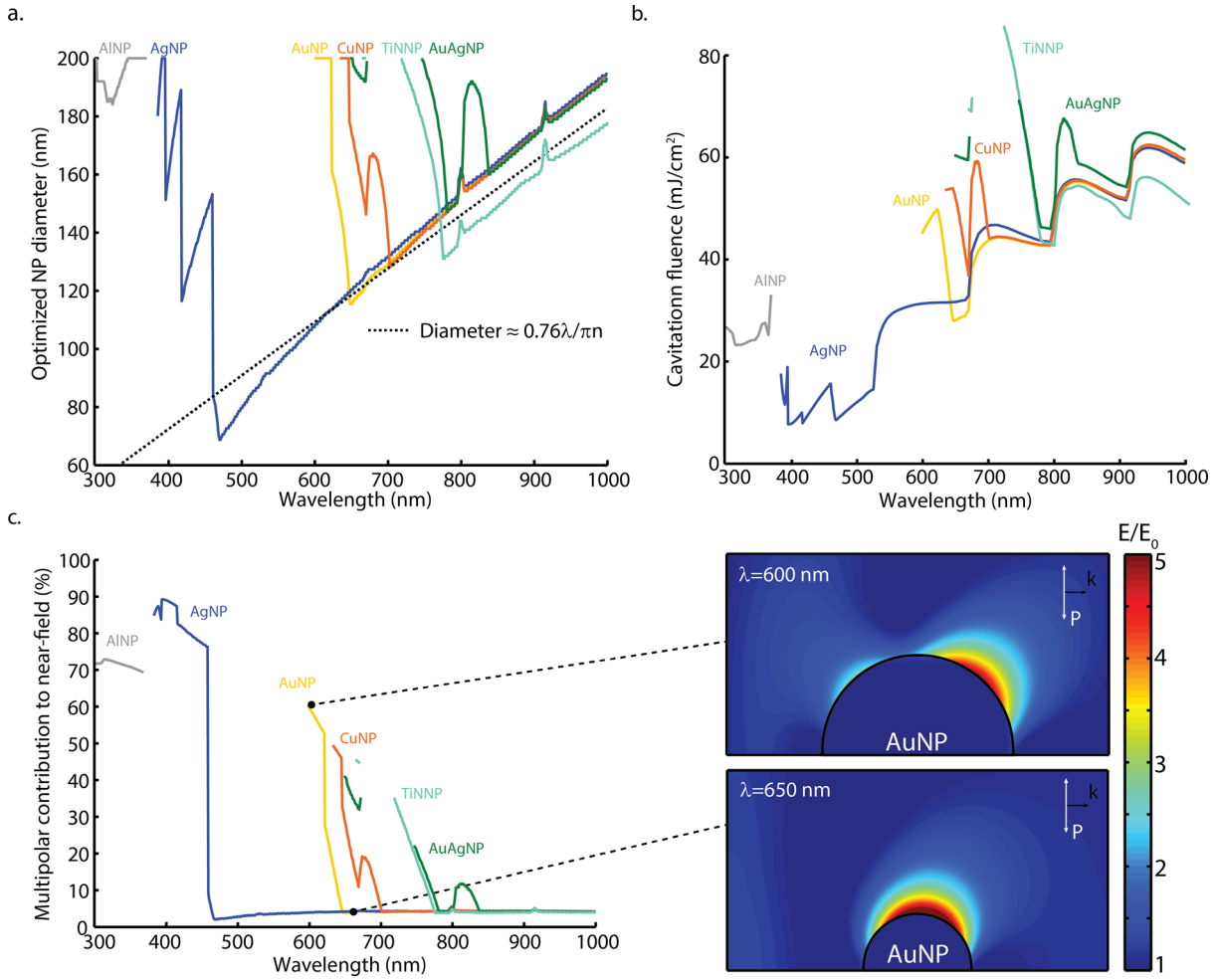

Figure 4. Impact of the choice of material for designing optimal NP. (a) Optimal NP diameter for each material as a function of wavelength. When no line is present, cavitation cannot be induced without damaging the particle at this wavelength for this material. Ni, Ti, and Pt are not shown because no solution exists at any wavelength. (b) Corresponding cavitation thresholds. (c) Multipolar contributions to the near-field enhancement for optimized NP. Inset shows characteristic examples of mostly dipolar and mostly multipolar interaction with optimal AuNP.

spectra (649−672 and 747−1000 nm for AuAgNP and 665−671 and 719−1000 nm for TiNNP) due to the damage constraint.

In the UV−visible (300−700 nm), the cavitation enhancement and optimal NP size are highly material dependent (Figure 4a). These optima are heavily influenced by the thermal properties of the NP since energy absorption is very important at these wavelengths. Optimal NP often get bigger to keep the absorbed energy density below the damage threshold, resulting in increased multipolar interactions. This is apparent in Figure 4c that shows the multipolar contribution to the field enhancement for all materials. Notably, an almost purely dipolar behavior is shown for Ag at wavelength as short as 450 nm, due to very low resistive losses. This makes AgNP particularly well-suited for cavitation in the UV−visible (384−700 nm). AlNP can extend the feasible range into the UV (300−368 nm), but with reduced efficiency.

In the NIR (700−1000 nm), the differences between the cavitation enhancement of the various materials are greatly reduced, and the optimal cavitation thresholds are very similar for Ag, TiN, Cu, and Au and only slightly higher for AuAg. Interestingly, the optimal diameter for all materials in the NIR is also very similar and can again be approximated by $D \sim \lambda/5$. This behavior is due to the fact that the balance between damped polarizability and enhanced dipole emission is mostly geometrical and weakly depends on the dielectric function for materials with large negative permittivity, characteristic of metals in the NIR (SI, Supporting Note 1). In consequence, the durability window is the only property that significantly varies with materials for plasmon-enhanced cavitation in the NIR. Due to their high melting temperature, TiNNP are shown to be the most efficient NP for wavelengths larger than 815 nm.

Nanoshells and Multishells. In addition to size and materials, the geometry of the particles greatly influences their plasmon resonance characteristic and thermal behavior. Therefore, we wanted to evaluate how designing silica-metal nanoshells (NS) could yield better nanomaterials for plasmon-enhanced nanocavitation. In a previous work, we have shown how the extra-tunability of AuNS (obtained by carefully adjusting the silica core radius and shell thickness) could yield nanomaterials optimized for cavitation and cell optoporation in the NIR.[37] This unique tunability has also been used by other groups for enhanced biosensing,[51] gene silencing,[52] cancer treatment,[53] DNA release,[54] and steam production.[55,56]

Using our computational framework, we optimized the cavitation threshold and durability window for NS made of a silica core with a single metallic layer, considering all metals

DOI: 10.1021/acsphotonics.6b00652
ACS Photonics XXXX, XXX, XXX−XXX

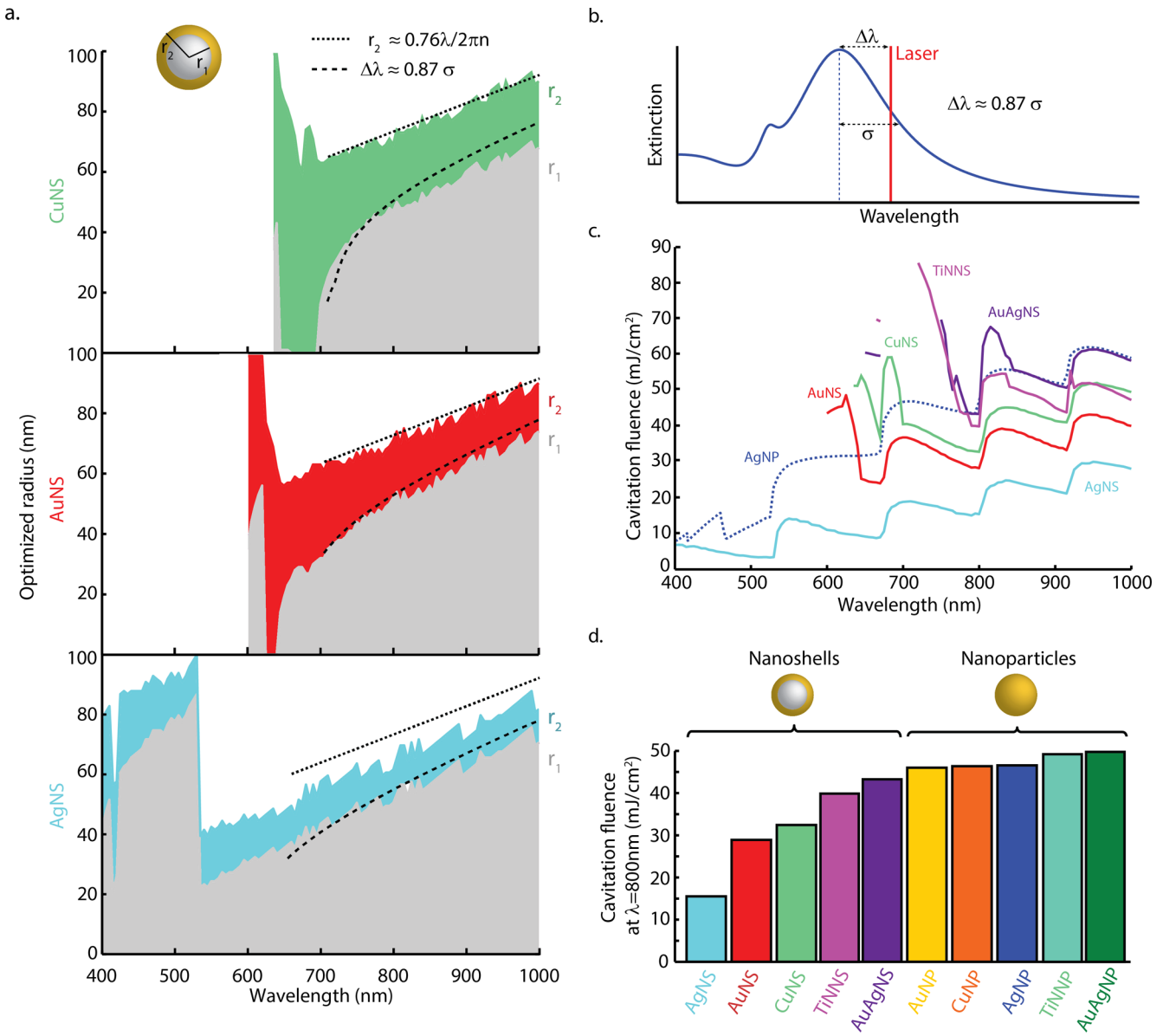

Figure 5. Optimal NS for various metallic compositions. (a) Optimal NS inner core radius (in gray) and total outer radius (in color) for CuNS, AuNS, and AgNS. Blank regions indicate that no design leading to cavitation without damage exists. Dash lines indicate the guidelines for the optimal inner core radius ($\Delta\lambda = 0.87\sigma$) and the outer radius ($r_2 \sim 0.76\lambda/2\pi n$). (b) Determination of the optimal inner core radius. The difference between the extinction peak and laser irradiation wavelengths ($\Delta\lambda$) must be 0.87 times the half width at half-maximum (σ) of the extinction peak in order to reach optimality. (c) Optimal cavitation fluence threshold for all tested NS as a function of the irradiation wavelength. (d) Cavitation fluence threshold for optimal NS and NP at λ = 800 nm.

that were tested above for NP. The maximal outer diameter for NS was set to 200 nm, and the inner core radius could be varied freely, with a resolution of 1 nm. Irradiation wavelengths have been tested for λ = 300−1000 nm with increments of 5 nm. Our results show that NS do not extend the durability window for any metal tested. Similar to the case of NP, PtNS and NiNS cannot yield durable nanoantennas across the UV−visible and NIR, for any combination of core radius and shell thickness. However, due to spectral tunability, F_{bubble} are respectively reduced by up to 86, 39, 49, and 17% for AgNS, AuNS, CuNS, and AuAgNS compared to their corresponding optimized NP. For some portions of the irradiation spectrum, the best NS is in reality a NP, their core radius being reduced to zero. For instance, this occurs for AuNS in the 625−640 nm range (Figure 5a). Notably, optimal AlNS are always NP (inner diameter of 0), although nonoptimal durable AlNS also exist, in opposition to NiNS and PtNS that cannot induce cavitation without sustaining damage for any combinations of core radius and shell thicknesses (Figure S1).

Analogous to NP, the sizes of optimal NS are shown to follow simple rules that depend of the irradiation wavelength. In the NIR, the outer diameter of the optimal NS approximately follows the $D \sim \lambda/5$ guideline that was previously deduced for NP (Figure 5a). This behavior is not surprising, given the fact that the near-field enhancement is essentially dipolar. As in the case of NP, the size dependence of the polarizability leads to a similar trend. We can also determine a guideline for the optimal diameter of the inner silica core. As shown on Figure 5b, a simple nonlinear regression procedure (SI, Supporting Note 2) shows that the

DOI: 10.1021/acsphotonics.6b00652
ACS Photonics XXXX, XXX, XXX−XXX

optimal inner diameter corresponds to a spectral response in which the spectral distance between the irradiation wavelength and the extinction cross-section peak is 0.87 times its half width at half-maximum ($\Delta\lambda = 0.87\sigma$), which seems to provide the right balance of field enhancement and density of energy absorption. This general rule can serve as a guideline for the design of NS. Combined together, these two guidelines ($D \sim \lambda/5$ for the outer diameter, and $\Delta\lambda = 0.87\sigma$ for the inner diameter) uniquely define the optimal nanoshell in the NIR regime. Note that AuAgNS and TiNNS present an outer layer that is slightly thicker than expected, probably due to their higher absorptivity in the NIR compared to other metals (Figure S2).

Our results show that AgNS are the most efficient particles to durably induce cavitation. Indeed, AgNS exhibit the lowest F_{bubble} between all the NP and NS tested, across all wavelengths (Figure 5c). The optimal AgNS has a 86 nm silica core radius with a 13 nm thick Ag shell. Irradiated at $\lambda = 525$ nm, this particle presents a F_{bubble} of ~3.4 mJ/cm^2, two times better than the lowest threshold that could be achieved with AgNP (~8 mJ/cm^2 at $\lambda = 397$ nm) and seven times better than that of the best AuNS (~24 mJ/cm^2 at $\lambda = 670$ nm). At $\lambda = 800$ nm, a wavelength commonly used in ultrafast laser technology, all studied NS showed better performance than NP (Figure 5d). At this wavelength, AgNS again presents the lowest F_{bubble} with ~15 mJ/cm^2 (50 nm silica core radius with 11 nm thick silver layer). This is three times better than the lowest threshold that could be achieved with AgNP (~43 mJ/cm^2 at $\lambda = 800$ nm) and two times better than the best AuNS (28 mJ/cm^2 at $\lambda = 800$ nm).

Although Ag perform significantly better than all other metals, Au is generally preferred over Ag in biological applications, due to better stability, resistance to oxidation, and biocompatibility.[57−59] To overcome these limitations, AgNS can be coated with a thin Au layer (~1 nm; Figure S3), as previously reported.[60] Our computational framework suggests that this type of coating does not significantly degrade AgNS performance ($F_{bubble} \sim 18$ mJ/cm^2 at $\lambda = 800$ nm, compared to 15 mJ/cm^2 at $\lambda = 800$ nm for noncoated AgNS), while avoiding the problematic exposition of the Ag surface to the environment.

We next proceeded to test whether more complex layered spherical structures could yield durable nanoantennas with enhanced properties in the NIR compared to simple NP and NS. Using our computational methodology, we tested multishell systems (n-MS) composed of alternated layers of metal and silica. Structures with $n = 1−5$ Ag and Au layers were tested at $\lambda = 800$ nm, $n = 1$ and 2 corresponding to NP and NS, respectively. Results show that optimal 5-AgMS and 5-AuNS reduce F_{bubble} by 7 and 2% compared to AgNS and AuNS, respectively (Figure 6a). F_{bubble} saturates very rapidly when the number of layers n is increased, which brings very limited interest for structures with more than five layers. The geometry of all optimal n-MS are shown in Figure 6b. Similar to NS and NP, the outer diameter of optimal n-MS structures are shown to follow approximately the $D \sim \lambda/5$ guideline at 800 nm. The thicknesses of the different layers are adjusted to tune the extinction spectrum in a way that is very similar to NS, the plasmon resonance being blue-shifted relative to the laser irradiation ($\Delta\lambda$) with a constant value close to 0.87σ (Figure 6c). It is finally interesting to note that, for n-MS, energy absorption within the outer metallic layer is the most critical source of structural damage. In all cases, including NS, the melting temperature is reached in this layer before optical breakdown occurs in one of the inner silica layer. However, given the effort required to grow such complex multilayered structure, the potential of n-MS for enhanced cavitation is extremely limited.

a.

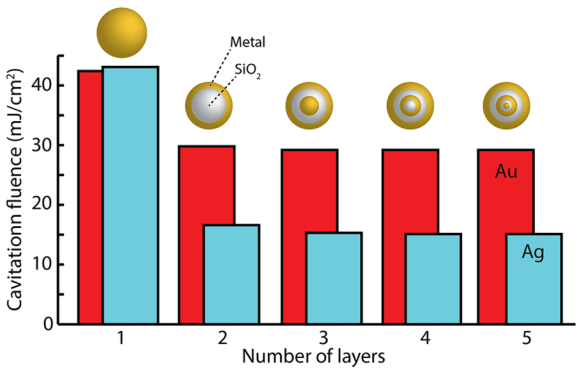

b.

Number of layers	Optimized AuMS ($r_1/r_2/r_3/...$) (nm)	Optimized AgMS ($r_1/r_2/r_3/...$) (nm)
1	75	76
2	52/71	50/61
3	24/50/70	23/50/62
4	4/24/50/70	8/23/50/62
5	3/4/24/50/70	5/8/23/50/62

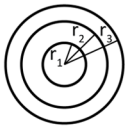

c.

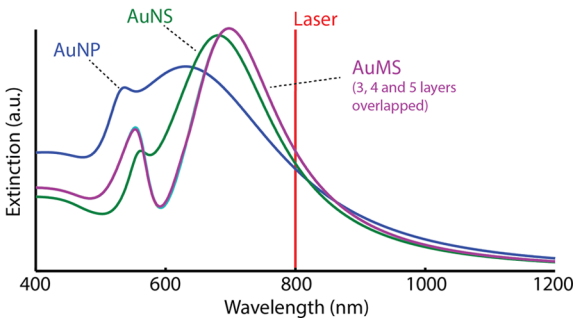

Figure 6. Optimal n-AuMS and n-AgMS with 1−5 layers. (a) Cavitation fluence threshold for Au (red) and Ag (blue) n-MS as a function of the number of layers. (b) Optimal sizes of the corresponding n-MS. (c) Comparison of the extinction spectra of the optimal AuNP, AuNS, and AuMS for an irradiation of $\lambda = 800$ nm.

CONCLUSIONS

In conclusion, we have developed a computational framework that is capable of screening large libraries of plasmonic nanostructures of different shapes, sizes, and compositions to design durable nanoantennas for plasmon-enhanced nanocavitation. These antennas enable reducing the laser fluence needed to initiate cavitation in liquid, while avoiding structural damage that would hinder multipulse and scanning procedures. The major findings of this work are summarized in Figure 7, which shows, for all tested materials, which particle size and irradiation wavelength can be used in the UV−visible and NIR to design durable NP (Figure 7a) and NS (Figure 7b) for nanocavitation. The optimal structures are also indicated in each case. Globally, AgNS are shown to be the best materials, with irradiation at $\lambda = 525$ nm, for which $F_{bubble} \sim 3.4$ mJ/cm^2.

DOI: 10.1021/acsphotonics.6b00652
ACS Photonics XXXX, XXX, XXX−XXX

a.

Nanoparticles

	UV-Visible (300-700nm)					NIR (700-1000nm)				
	Diameter (nm)		Wavelength (nm)		Fluence (mJ/cm²)	Diameter (nm)		Wavelength (nm)		Fluence (mJ/cm²)
	Feasible	Optimal	Feasible	Optimal	Optimal	Guideline	Optimal	Feasible	Optimal	Optimal
Ag	Material dependent (Figure 5a)	156	384-700	397	8	D ≈ λ/5	152	700-1000	795	43
Au		115	600-700	648	28		151	700-1000	795	43
Cu		138	635-700	670	37		150	700-1000	795	43
AuAg		192	649-672	668	59		150	747-1000	795	46
TiN		200	665-671	670	69		135	719-1000	795	43
Al		185	300-368	317	23					
Ni										
Pt										
Ti										

b.

Nanoshells

	UV-Visible (300-700nm)					NIR (700-1000nm)				
	Radius (r_1/r_2) (nm)		Wavelength (nm)		Fluence (mJ/cm²)	Radius (r_1/r_2) (nm)		Wavelength (nm)		Fluence (mJ/cm²)
	Feasible	Optimal	Feasible	Optimal	Optimal	Guidelines	Optimal	Feasible	Optimal	Optimal
Ag	Material dependent (Figure 6a)	84/97	384-700	525	3	D ≈ λ/5 Δλ ≈ 0.87σ	49/60	700-1000	790	15
Au		29/58	599-700	670	24		52/71	700-1000	800	28
Cu		0/69	635-700	670	37		47/69	700-1000	800	33
AuAg		0/96	649-672	668	59		31/75	747-1000	800	43
TiN		0/100	665-671	670	69		28/66	719-1000	800	40
Al		0/93	300-368	317	23					
Ni										
Pt										
Ti										

Figure 7. Summary of the major findings. (a) NP and (b) NS feasible and optimized sizes and wavelengths for all studied materials in the UV–visible and NIR. The cavitation fluences for the optimal particle size irradiated at optimal wavelength are also indicated.

This type of large-scale systematic survey would have been impossible to conduct using only experimental methods. Our computational methodology thus enables to efficiently guide experimentalists toward the most promising materials and structure, and to extract general guidelines for the design of new nanomaterial devices. While this current work is limited to spherical nanoparticles, our methodology could be extended to other 3D nanoshapes, including nanorods,[61−63] nanostars,[64−66] nanodisks,[67] or nanocages.[68−71] Because these no longer exhibit spherical symmetry, more advanced numerical methods would have to be employed to calculate the needed cross sections and near-field enhancement, such as DDA,[72,73] BEM,[74] FDTD,[65,75,76] or FEM.[76] More advanced physics-based theory that can predict the onset of cavitation or structural damage with more precision could also be used to improve the quantitative predictability of our modeling framework.[42] However, while possible, all these refinements would require a longer computing time that must be delicately balanced with the needed level of accuracy. While these problems are challenging, our work paves the way toward the development of nanoplasmonic material design methods that will soon become unavoidable for the efficient development of new nanoplasmonic devices.

METHODS

Modeling Overview and Limitations. Our objective, in this work, is to design nanoparticles that can generate bubbles upon ultrafast irradiation without being damaged. We thus developed models to estimate both the cavitation and the damage thresholds.

First, we compute the optical properties of the NP to determine the near-field enhancement, the near-field penetration depth and the absorption cross-section. These properties are essential to the determination of the cavitation and damage thresholds.

Second, we calculate the plasma generation associated with the onset of bubble formation. The near-field enhancement and penetration depth are used to calculate this plasma generation into the near-field volume. It is then possible to deduce the laser fluence needed to reach a plasma density of 10^{21} cm^{-3}, which we define as the condition for cavitation threshold. This hypothesis is only valid if plasma generation in the water is the dominant physical mechanism leading to cavitation over thermal effects due to NP absorption. Since our objective is to limit the absorption, this hypothesis should be valid for all NPs and irradiation conditions considered. For the same reason, hot electrons ejected from the NP are also neglected.

Finally, we calculate the temperature rise into the NP metal using the absorption cross-section and the thermodynamic properties of the metal. We assume that all the laser energy absorbed by the NP is transferred into heat in the metal without any loss. This hypothesis is only valid if the laser irradiation is shorter than the heat diffusion time, which is always the case in this work for ultrafast laser pulses. It is then possible to deduce the laser fluence needed to reach melting temperature inside the NP, which is taken as the damage threshold.

Computation of the Optical Properties of Plasmonic Nanoparticles. NP optical properties were computed using the Mie solution of the Maxwell's equations.[77,78] An in-house code (NFMieCoated) was developed to compute the absorption, scattering, and extinction cross sections, as well as the near-field enhancement and distribution around spherical NP, NS, and MS irradiated by plane waves at a given wavelength. Our Mie solution involves expanding the electromagnetic fields into infinite series of spherical vector wave

DOI: 10.1021/acsphotonics.6b00652
ACS Photonics XXXX, XXX, XXX−XXX

functions and using the boundary conditions at interfaces to solve the Maxwell's equations for the complete field.[78] Our code is available in the Supporting Data as a MATLAB function (SI, Supporting Note 3). The real and imaginary parts of the refractive indexes as a function of the irradiation wavelength have been taken from tabulated data for all the materials and are shown in Figure S4.

Four characteristic parameters were evaluated using the NFMieCoated code: (1) The absorption cross-section (C_{abs}) of each metallic layers composing the particle, (2) the maximal near-field enhancement in the silica (NFE_{SiO_2}) (when present), (3) the maximal near-field enhancement in the water (NFE), and (4) the penetration length (L) of the near-field into the surrounding water. In this work, L was defined as the full width at half-maximum of the radial NFE, taken at the angular position that corresponds to the maximal NFE.

Computation of the Cavitation Fluence Threshold. Computation of the fluence threshold for cavitation was based on the calculation of the density of the plasmon-enhanced plasma generation in the near-field. A plasma density threshold of $\rho = 10^{21}$ cm^{-3} was used, in agreement with previous studies of laser-induced cavitation in water.[38−40] To calculate the plasma density, we used a rate equation that account for the plasma creation through multiphotonic and collision mechanisms and the plasma decrease through charge recombination and diffusion. The computation of the plasma density around the NP is given by[38]

$$\frac{\partial \rho}{\partial t} = S_{photo} + S_{coll}\rho - S_{rec}\rho^2 - S_{diff}\rho \tag{1}$$

with S_{photo}, the Keldysh photoionization rate in strong fields that describes the plasma formation through multiphotonic and tunnel ionization,[79] S_{coll}, the collision rate that describes the plasma formation through impact ionization, S_{rec} the recombination rate of the excited charges to water molecules fundamental state, and S_{diff} the diffusion rate of the charges outside the near-field volume. Explicit expressions for S_{photo} and S_{rec} can be found elsewhere.[37] The collision rate, S_{coll}, is given by

$$S_{coll} = \begin{cases} \dfrac{\eta}{1 + \eta \cdot \tau_{coll} n}, & \text{for } \rho V \geq 0.5 \\ 0, & \text{for } \rho V < 0.5 \end{cases} \tag{2}$$

where τ_{coll} is the time between collisions (1.7 fs[80]), n is the number of photons required to give the electrons 1.5 times the gap energy, V is the volume in which electrons are excited, and η is the ionization rate per electron and is given by

$$\eta = \frac{1}{\omega^2 {\tau_{coll}}^2 + 1}\left(\frac{e^2 \tau_{coll} |E|^2}{m_e [3/2]\Delta} + \frac{m_e \omega^2 \tau_{coll}}{M}\right) \tag{3}$$

where ω is the light radial frequency, E is the electromagnetic field, Δ is the effective ionization potential (~6.5 eV for water[38]), and M the mass of a water molecule. We defined the volume V as a sphere of radius L, where L is the penetration length of the near-field into the surrounding water.

Finally, the diffusion rate S_{diff} is given by

$$S_{diff} = \frac{\tau_{coll}[5/4]\Delta}{3 m_{eq} L^2} \tag{4}$$

m_{eq} is the exciton reduced mass, given by $1/m_{eq} = 1/m_e + 1/m_h$, where m_e and m_h are the effective mass of the quasi-free electron in the conduction band and the hole in the valence band, respectively.

Equation 1 was solved in Matlab (Mathwork Inc., Burlington) using the ode15s solver. The fsolve routine was used to find the laser fluence required to reach $\rho = 10^{21}$ cm^{-3}. This fluence is then divided by $|NFE|^2$ to find F_{bubble}.

Computation of the Structural Damage Fluence Threshold. The fluence threshold for structural damage (F_{damage}) was determined from the minimum value between the fluence required to reach the melting temperature of each metallic layer (F_{melt}) and the fluence required to reach breakdown in each silica layers (F_{SiO_2}), if present. F_{melt} was calculated using

$$F_{melt} = \frac{m c_p (T_{melt} - T_0)}{C_{abs}} \tag{5}$$

m is the mass of metal in each layer, c_p is the specific heat of metal at constant pressure, and T_{melt} and T_0 are the melting temperature of the metal and the room temperature, respectively. The values of c_p and T_{melt} used for each metal can be found in Figure S5. The threshold for optical breakdown in silica has been estimated to 3.92 J/cm^2 using eq 1 for a large laser focal spot size (>1 μm) and an irradiation wavelength of 800 nm. This value was divided by $|NFE_{SiO_2}|^2$ in each silica layer to yield F_{SiO_2}.

■ ASSOCIATED CONTENT

Supporting Information

The Supporting Information is available free of charge on the ACS Publications website at DOI: 10.1021/acsphotonics.6b00652.

Supporting note 1: derivation of the material independence of the maximal near-field in the long-wavelength limit; Supporting note 2: design guideline for the inner core radius of nanoshells; Supporting note 3: NFMieCoated matlab function for calculating the optical properties of spherical multishell nanostructures; supporting figures and references (PDF).

NFMieCoated MATLAB function (TXT).

■ AUTHOR INFORMATION

Corresponding Author

*E-mail: michel.meunier@polymtl.ca.

Author Contributions

R.L. developed the computational design method, developed the cavitation and structural damage model, optimized the NP, NS, and MS for all materials, and analyzed all data; E.B. developed the plasma generation model and analyzed data; D.R. developed and provided the NFMieCoated code; C.B. provided the experimental cavitation thresholds; M.M. supervised the work and analyzed all data. R.L., E.B., D.R., and M.M. wrote the manuscript; and all authors edited, commented, and approved the final version of the manuscript.

Notes

The authors declare no competing financial interest.

DOI: 10.1021/acsphotonics.6b00652
ACS Photonics XXXX, XXX, XXX−XXX

■ ACKNOWLEDGMENTS

The authors acknowledge the Natural Science and Engineering Research Council (NSERC) and Le Fond Québecois de la Recherche sur la Nature et les Technologies (FQRNT) for fundings. C.B. acknowledges funding from the EU under a Marie Curie Fellowship, FP7-PEOPLE-2013-IOF, Project Reference 624888. Adrien Dagallier, Vi Tching de Lille, Nicolas Le Hir, and Éric Bergeron are acknowledged for valuable discussions. Yves Drolet is acknowledged for technical support.

■ REFERENCES

(1) Berweger, S.; Atkin, J. M.; Xu, X. G.; Olmon, R. L.; Raschke, M. B. Femtosecond Nanofocusing with Full Optical Waveform Control. *Nano Lett.* **2011**, *11*, 4309−4313.

(2) Novotny, L.; van Hulst, N. Antennas for Light. *Nat. Photonics* **2011**, *5*, 83−90.

(3) Plech, A.; Kotaidis, V.; Lorenc, M.; Boneberg, J. Femtosecond Laser near-Field Ablation from Gold Nanoparticles. *Nat. Phys.* **2006**, *2*, 44−47.

(4) Brongersma, M. L.; Halas, N. J.; Nordlander, P. Plasmon-Induced Hot Carrier Science and Technology. *Nat. Nanotechnol.* **2015**, *10*, 25−34.

(5) McFarland, A. D.; Van Duyne, R. P. Single Silver Nanoparticles As Real Time Optical Sensors With Zeptomole Sensitivity. *Nano Lett.* **2003**, *3*, 1057−1062.

(6) Vendrell, M.; Maiti, K. K.; Dhaliwal, K.; Chang, Y.-T. Surface-Enhanced Raman Scattering in Cancer Detection and Imaging. *Trends Biotechnol.* **2013**, *31*, 249−257.

(7) Lozano, N.; Al-Jamal, W. T.; Taruttis, A.; Beziere, N.; Burton, N. C.; Van Den Bossche, J.; Mazza, M.; Herzog, E.; Ntziachristos, V.; Kostarelos, K. Liposome-Gold Nanorod Hybrids for High-Resolution Visualization Deep in Tissues. *J. Am. Chem. Soc.* **2012**, *134*, 13256−13258.

(8) Mallidi, S.; Larson, T.; Tam, J.; Joshi, P. P.; Karpiouk, A.; Sokolov, K.; Emelianov, S. Multiwavelength Photoacoustic Imaging and Plasmon Resonance Coupling of Gold Nanoparticles for Selective Detection of Cancer. *Nano Lett.* **2009**, *9*, 2825−2831.

(9) Atwater, H. A.; Polman, A. Plasmonics for Improved Photovoltaic Devices. *Nat. Mater.* **2010**, *9*, 205−213.

(10) Yavuz, M. S.; Cheng, Y.; Chen, J.; Cobley, C. M.; Zhang, Q.; Rycenga, M.; Xie, J.; Kim, C.; Song, K. H.; Schwartz, A. G.; Wang, L. V.; Xia, Y. Gold Nanocages Covered by Smart Polymers for Controlled Release with near-Infrared Light. *Nat. Mater.* **2009**, *8*, 935−939.

(11) Rwei, A. Y.; Wang, W.; Kohane, D. S. Photoresponsive Nanoparticles for Drug Delivery. *Nano Today* **2015**, *10*, 451−467.

(12) Stockman, M. I. Nanoplasmonics: Past, Present, and Glimpse into Future. *Opt. Express* **2011**, *19*, 22029−22106.

(13) Knight, M. W.; King, N. S.; Liu, L.; Everitt, H. O.; Nordlander, P.; Halas, N. J. Aluminum for Plasmonics. *ACS Nano* **2014**, *8*, 834−840.

(14) Sundararaman, R.; Narang, P.; Jermyn, A. S.; Goddard, W. A., III; Atwater, H. A. Theoretical Predictions for Hot-Carrier Generation from Surface Plasmon Decay. *Nat. Commun.* **2014**, *5*, 5788.

(15) Brown, A. M.; Sundararaman, R.; Narang, P.; Goddard, W. A.; Atwater, H. A. Non-Radiative Plasmon Decay and Hot Carrier Dynamics: Effects of Phonons, Surfaces and Geometry. *ACS Nano* **2016**, *10*, 957−966.

(16) Zhou, L.; Zhang, C.; McClain, M. J.; Manjavacas, A.; Krauter, C. M.; Tian, S.; Berg, F.; Everitt, H. O.; Carter, E. A.; Nordlander, P.; Halas, N. J. Aluminum Nanocrystals as a Plasmonic Photocatalyst for Hydrogen Dissociation. *Nano Lett.* **2016**, *16*, 1478−1484.

(17) Chan, G. H.; Zhao, J.; Hicks, E. M.; Schatz, G. C.; Duyne, R. P. Van. Plasmonic Properties of Copper Nanoparticles Fabricated by Nanosphere Lithography. *Nano Lett.* **2007**, *7*, 1947−1952.

(18) Wang, H. Y.; Lua, A. C. Development of Metallic Nickel Nanoparticle Catalyst for the Decomposition of Methane into Hydrogen and Carbon Nanofibers. *J. Phys. Chem. C* **2012**, *116*, 26765−26775.

(19) Zhang, W.; Zhang, X.; Zhang, L.; Chen, G. Fabrication of Carbon Nanotube-Nickel Nanoparticle Hybrid Paste Electrodes for Electrochemical Sensing of Carbohydrates. *Sens. Actuators, B* **2014**, *192*, 459−466.

(20) Joo, S. H.; Choi, S. J.; Oh, I.; Kwak, J.; Liu, Z.; Terasaki, O.; Ryoo, R. Ordered Nanoporous Arrays of Carbon Supporting High Dispersions of Platinum Nanoparticles. *Nature* **2001**, *412*, 169−172.

(21) Naik, G. V.; Schroeder, J. L.; Ni, X.; Kildishev, A. V.; Sands, T. D.; Boltasseva, A. Titanium Nitride as a Plasmonic Material for Visible and near-Infrared Wavelengths. *Opt. Mater. Express* **2012**, *2*, 478−489.

(22) Kaskel, S.; Schlichte, K.; Chaplais, G.; Khanna, M. Synthesis and Characterisation of Titanium Nitride Based Nanoparticles. *J. Mater. Chem.* **2003**, *13*, 1496.

(23) Guler, U.; Ndukaife, J. C.; Naik, G. V.; Nnanna, A. G. A.; Kildishev, A. V.; Shalaev, V. M.; Boltasseva, A. Local Heating with Lithographically Fabricated Plasmonic Titanium Nitride Nanoparticles. *Nano Lett.* **2013**, *13*, 6078−6083.

(24) Link, S.; Wang, Z. L.; El-Sayed, M. a. Alloy Formation of Gold-Silver Nanoparticles and the Dependence of the Plasmon Absorption on Their Composition. *J. Phys. Chem. B* **1999**, *103*, 3529−3533.

(25) Rioux, D.; Vallières, S.; Besner, S.; Munoz, P.; Mazur, E.; Meunier, M. An Analytic Model for the Dielectric Function of Au, Ag, and Their Alloys. *Adv. Opt. Mater.* **2014**, *2*, 176−182.

(26) Rioux, D.; Meunier, M. Seeded Growth Synthesis of Composition and Size-Controlled Gold−Silver Alloy Nanoparticles. *J. Phys. Chem. C* **2015**, *119*, 13160−13168.

(27) Patskovsky, S.; Bergeron, E.; Rioux, D.; Simard, M.; Meunier, M. Hyperspectral Reflected Light Microscopy of Plasmonic Au/Ag Alloy Nanoparticles Incubated as Multiplex Chromatic Biomarkers with Cancer Cells. *Analyst* **2014**, *139*, 5247−5253.

(28) Dallaire, A. M.; Rioux, D.; Rachkov, A.; Patskovsky, S.; Meunier, M. Laser-Generated Au-Ag Nanoparticles for Plasmonic Nucleic Acid Sensing. *J. Phys. Chem. C* **2012**, *116*, 11370−11377.

(29) Boulais, É.; Lachaine, R.; Meunier, M. Plasma Mediated off-Resonance Plasmonic Enhanced Ultrafast Laser-Induced Nanocavitation. *Nano Lett.* **2012**, *12*, 4763−4769.

(30) Lachaine, R.; Boulais, É.; Meunier, M. From Thermo- to Plasma-Mediated Ultrafast Laser-Induced Plasmonic Nanobubbles. *ACS Photonics* **2014**, *1*, 331−336.

(31) Boulais, E.; Lachaine, R.; Hatef, A.; Meunier, M. Plasmonics for Pulsed-Laser Cell Nanosurgery: Fundamentals and Applications. *J. Photochem. Photobiol., C* **2013**, *17*, 26−49.

(32) Lukianova-Hleb, E. Y.; Kim, Y.-S.; Belatsarkouski, I.; Gillenwater, A. M.; O'Neill, B. E.; Lapotko, D. O. Intraoperative Diagnostics and Elimination of Residual Microtumours with Plasmonic Nanobubbles. *Nat. Nanotechnol.* **2016**, *11*, 25−28.

(33) Lukianova-Hleb, E. Y.; Ren, X.; Sawant, R. R.; Wu, X.; Torchilin, V. P.; Lapotko, D. O. On-Demand Intracellular Amplification of Chemoradiation with Cancer-Specific Plasmonic Nanobubbles. *Nat. Med.* **2014**, *20*, 778−784.

(34) Baumgart, J.; Humbert, L.; Boulais, É.; Lachaine, R.; Lebrun, J. J.; Meunier, M. Off-Resonance Plasmonic Enhanced Femtosecond Laser Optoporation and Transfection of Cancer Cells. *Biomaterials* **2012**, *33*, 2345−2350.

(35) Schaeublin, N. M.; Braydich-Stolle, L. K.; Schrand, A. M.; Miller, J. M.; Hutchison, J.; Schlager, J. J.; Hussain, S. M. Surface Charge of Gold Nanoparticles Mediates Mechanism of Toxicity. *Nanoscale* **2011**, *3*, 410−420.

(36) Bisker, G.; Yelin, D. Noble-Metal Nanoparticles and Short Pulses for Nanomanipulations: Theoretical Analysis. *J. Opt. Soc. Am. B* **2012**, *29*, 1383.

(37) Lachaine, R.; Boutopoulos, C.; Lajoie, P.-Y.; Boulais, É.; Meunier, M. Rational Design of Plasmonic Nanoparticles for Enhanced Cavitation and Cell Perforation. *Nano Lett.* **2016**, *16*, 3187−3194.

DOI: 10.1021/acsphotonics.6b00652
ACS Photonics XXXX, XXX, XXX−XXX

(38) Vogel, A.; Noack, J.; Hüttman, G.; Paltauf, G. Mechanisms of Femtosecond Laser Nanosurgery of Cells and Tissues. *Appl. Phys. B: Lasers Opt.* **2005**, *81*, 1015−1047.
(39) Stuart, B.; Feit, M.; Herman, S.; Rubenchik, a.; Shore, B.; Perry, M. Nanosecond-to-Femtosecond Laser-Induced Breakdown in Dielectrics. *Phys. Rev. B: Condens. Matter Mater. Phys.* **1996**, *53*, 1749−1761.
(40) Noack, J.; Vogel, A. Laser-Induced Plasma Formation in Water at Nanosecond to Femtosecond Time Scales: Calculation of Thresholds, Absorption Coefficients, and Energy Density. *IEEE J. Quantum Electron.* **1999**, *35*, 1156−1167.
(41) Kennedy, P. K.; Hammer, D. X.; Rockwell, B. A. Laser-Induced Breakdown in Aqueous Media. *Prog. Quantum Electron.* **1997**, *21*, 155−248.
(42) Dagallier, A.; Boulais, É.; Boutopoulos, C.; Lachaine, R.; Meunier, M. Multiscale Modeling of Plasmonic Enhanced Energy Transfer and Cavitation around Laser-Excited Nanoparticles. *Nano Lett.* **2016**, submitted for publication.
(43) Link, S.; Burda, C.; Nikoobakht, B.; El-Sayed, M. A. Laser-Induced Shape Changes of Colloidal Gold Nanorods Using Femtosecond and Nanosecond Laser Pulses. *J. Phys. Chem. B* **2000**, *104*, 6152−6163.
(44) Takami, A.; Kurita, H.; Koda, S. Laser-Induced Size Reduction of Noble Metal Particles. *J. Phys. Chem. B* **1999**, *103*, 1226−1232.
(45) Boutopoulos, C.; Hatef, A.; Fortin-Deschênes, M.; Meunier, M. Dynamic Imaging of a Single Gold Nanoparticle in Liquid Irradiated by off-Resonance Femtosecond Laser. *Nanoscale* **2015**, *7*, 11758−11765.
(46) Zhigilei, L. V.; Lin, Z.; Ivanov, D. S. Atomistic Modeling of Short Pulse Laser Ablation of Metals: Connections between Melting, Spallation, and Phase Explosion. *J. Phys. Chem. C* **2009**, *113*, 11892−11906.
(47) Bulgakova, N. M.; Bulgakov, A. V. Pulsed Laser Ablation of Solids: Transition from Normal Vaporization to Phase Explosion. *Appl. Phys. A: Mater. Sci. Process.* **2001**, *73*, 199−208.
(48) Lorazo, P.; Lewis, L. J.; Meunier, M. Thermodynamic Pathways to Melting, Ablation, and Solidification in Absorbing Solids under Pulsed Laser Irradiation. *Phys. Rev. B: Condens. Matter Mater. Phys.* **2006**, *73*, 1−22.
(49) Linz, N.; Freidank, S.; Liang, X. X.; Vogelmann, H.; Trickl, T.; Vogel, A. Wavelength Dependence of Nanosecond Infrared Laser-Induced Breakdown in Water: Evidence for Multiphoton Initiation via an Intermediate State. *Phys. Rev. B: Condens. Matter Mater. Phys.* **2015**, *91*, 1−10.
(50) Eversole, D.; Luk'Yanchuk, B.; Ben-Yakar, A. Plasmonic Laser Nanoablation of Silicon by the Scattering of Femtosecond Pulses near Gold Nanospheres. *Appl. Phys. A: Mater. Sci. Process.* **2007**, *89*, 283−291.
(51) Hirsch, L. R.; Jackson, J. B.; Lee, A.; Halas, N. J.; West, J. L. A Whole Blood Immunoassay Using Gold Nanoshells. *Anal. Chem.* **2003**, *75*, 2377−2381.
(52) Huschka, R.; Barhoumi, A.; Liu, Q.; Roth, J. A.; Ji, L.; Halas, N. J. Gene Silencing by Gold Nanoshell-Mediated Delivery and Laser-Triggered Release of Antisense Oligonucleotide and siRNA. *ACS Nano* **2012**, *6*, 7681−7691.
(53) Gobin, A. M.; Lee, M. H.; Halas, N. J.; James, W. D.; Drezek, R. A.; West, J. L.; Gobin, M.; Lee, M. H.; Halas, N. J.; James, W. D.; Drezek, R. A.; West, J. L. Near-Infrared Resonant Nanoshells for Combined Optical Imaging and Photothermal Cancer Therapy. *Nano Lett.* **2007**, *7*, 1929−1934.
(54) Huschka, R.; Zuloaga, J.; Knight, M. W.; Brown, L. V.; Nordlander, P.; Halas, N. J. Light-Induced Release of DNA from Gold Nanoparticles: Nanoshells and Nanorods. *J. Am. Chem. Soc.* **2011**, *133*, 12247−12255.
(55) Neumann, O.; Neumann, A. D.; Silva, E.; Ayala-Orozco, C.; Tian, S.; Nordlander, P.; Halas, N. J. Nanoparticle-Mediated, Light-Induced Phase Separations. *Nano Lett.* **2015**, *15*, 7880−7885.
(56) Neumann, O.; Urban, A. S.; Day, J.; Lal, S.; Nordlander, P.; Halas, N. J. Solar Vapor Generation Enabled by Nanoparticles. *ACS Nano* **2013**, *7*, 42−49.
(57) Asharani, P. V.; Low Kah Mun, G.; Hande, M. P.; Valiyaveettil, S. Cytotoxicity and Genotoxicity of Silver Nanoparticles in Human Cells. *ACS Nano* **2009**, *3*, 279−290.
(58) Asharani, P. V.; Lianwu, Y.; Gong, Z.; Valiyaveettil, S. Comparison of the Toxicity of Silver, Gold and Platinum Nanoparticles in Developing Zebrafish Embryos. *Nanotoxicology* **2011**, *5*, 43−54.
(59) Bar-Ilan, O.; Albrecht, R. M.; Fako, V. E.; Furgeson, D. Y. Toxicity Assessments of Multisized Gold and Silver Nanoparticles in Zebrafish Embryos. *Small* **2009**, *5*, 1897−1910.
(60) Gao, C.; Goebl, J.; Yin, Y. Seeded Growth Route to Noble Metal Nanostructures. *J. Mater. Chem. C* **2013**, *1*, 3898−3909.
(61) Pérez-Juste, J.; Pastoriza-Santos, I.; Liz-Marzán, L. M.; Mulvaney, P. Gold Nanorods: Synthesis, Characterization and Applications. *Coord. Chem. Rev.* **2005**, *249*, 1870−1901.
(62) Huang, X.; Neretina, S.; El-Sayed, M. A. Gold Nanorods: From Synthesis and Properties to Biological and Biomedical Applications. *Adv. Mater.* **2009**, *21*, 4880−4910.
(63) Boulais, É.; Lachaine, R.; Meunier, M. Plasma-Mediated Nanocavitation and Photothermal Effects in Ultrafast Laser Irradiation of Gold Nanorods in Water. *J. Phys. Chem. C* **2013**, *117*, 9386−9396.
(64) Khoury, C. G.; Vo-Dinh, T. Gold Nanostars For Surface-Enhanced Raman Scattering: Synthesis, Characterization and Optimization. *J. Phys. Chem. C* **2008**, *112*, 18849−18859.
(65) Hao, F.; Nehl, C. L.; Hafner, J. H.; Nordlander, P. Plasmon Resonances of a Gold Nanostar. *Nano Lett.* **2007**, *7*, 729−732.
(66) Baginskiy, I.; Lai, T. C.; Cheng, L. C.; Chan, Y. C.; Yang, K. Y.; Liu, R. S.; Hsiao, M.; Chen, C. H.; Hu, S. F.; Her, L. J.; Tsai, D. P. Chitosan-Modified Stable Colloidal Gold Nanostars for the Photothermolysis of Cancer Cells. *J. Phys. Chem. C* **2013**, *117*, 2396−2410.
(67) Kuttge, M.; García De Abajo, F. J.; Polman, A. Ultrasmall Mode Volume Plasmonic Nanodisk Resonators. *Nano Lett.* **2010**, *10*, 1537−1541.
(68) Chen, J.; Yang, M.; Zhang, Q.; Cho, E. C.; Cobley, C. M.; Kim, C.; Glaus, C.; Wang, L. V.; Welch, M. J.; Xia, Y. Gold Nanocages: A Novel Class of Multifunctional Nanomaterials for Theranostic Applications. *Adv. Funct. Mater.* **2010**, *20*, 3684−3694.
(69) Chen, J.; Glaus, C.; Laforest, R.; Zhang, Q.; Yang, M.; Gidding, M.; Welch, M. J.; Xia, Y. Gold Nanocages as Photothermal Transducers for Cancer Treatment. *Small* **2010**, *6*, 811−817.
(70) Skrabalak, S. E.; Chen, J.; Au, L.; Lu, X.; Li, X.; Xia, Y. Gold Nanocages for Biomedical Applications. *Adv. Mater.* **2007**, *19*, 3177−3184.
(71) Chen, J.; Wiley, B.; Li, Z. Y.; Campbell, D.; Saeki, F.; Cang, H.; Au, L.; Lee, J.; Li, X.; Xia, Y. Gold Nanocages: Engineering Their Structure for Biomedical Applications. *Adv. Mater.* **2005**, *17*, 2255−2261.
(72) Draine, B. T. The Discrete-Dipole Approximation and Its Application to Interstellar Graphite Grains. *Astrophys. J.* **1988**, *333*, 848−872.
(73) Brioude, A.; Jiang, X. C.; Pileni, M. P. Optical Properties of Gold Nanorods: DDA Simulations Supported by Experiments. *J. Phys. Chem. B* **2005**, *109*, 13138−13142.
(74) García de Abajo, F. J.; Howie, A. Retarded Field Calculation of Electron Energy Loss in Inhomogeneous Dielectrics. *Phys. Rev. B: Condens. Matter Mater. Phys.* **2002**, *65*, 115418.
(75) Hao, F.; Nordlander, P. Efficient Dielectric Function for FDTD Simulation of the Optical Properties of Silver and Gold Nanoparticles. *Chem. Phys. Lett.* **2007**, *446*, 115−118.
(76) Jin, J.-M. *The Finite Element Method in Electromagnetics*; John Wiley & Sons, 2014.
(77) Mie, G. Beiträge Zur Optik Trüber Medien, Speziell Kolloidaler Metallösungen. *Ann. Phys.* **1908**, *330*, 377−445.
(78) Le Ru, E. C.; Etchegoin, P. G. *Principles of Surface Enhanced Raman Scattering and Related Plasmonic Effects*; Elsevier: Amsterdam, 2009.

DOI: 10.1021/acsphotonics.6b00652
ACS Photonics XXXX, XXX, XXX−XXX

(79) Keldysh, L. V. Ionization in the Field of a Strong Electromagnetic Wave. *J. Exp. Theor. Phys.* **1965**, *20*, 1307−1314.
(80) Sun, Q.; Jiang, H.; Liu, Y.; Wu, Z.; Yang, H.; Gong, Q. Measurement of the Collision Time of Dense Electronic Plasma Induced by a Femtosecond Laser in Fused Silica. *Opt. Lett.* **2005**, *30*, 320−322.

DOI: 10.1021/acsphotonics.6b00652
ACS Photonics XXXX, XXX, XXX−XXX